ADVANCED MATERIALS
www.advmat.de

Check for updates

Giant Spin Hall Effect and Spin–Orbit Torques in 5*d* Transition Metal–Aluminum Alloys from Extrinsic Scattering

*Peng Wang, Andrea Migliorini, See-Hun Yang, Jae-Chun Jeon, Ilya Kostanovskiy, Holger Meyerheim, Hyeon Han, Hakan Deniz, and Stuart S. P. Parkin**

The generation of spin currents from charge currents via the spin Hall effect (SHE) is of fundamental and technological interest. Here, some of the largest SHEs yet observed via extrinsic scattering are found in a large class of binary compounds formed from a 5*d* element and aluminum, with a giant spin Hall angle (SHA) of ≈1 in the compound $Os_{22}Al_{78}$. A critical composition of the 5*d* element is found at which there is a structural phase boundary between poorly and highly textured crystalline material, where the SHA exhibits its largest value. Furthermore, a systematic increase is found in the spin Hall conductivity (SHC) and SHA at this critical composition as the atomic number of the 5*d* element is systematically increased. This clearly shows that the SHE and SHC are derived from extrinsic scattering mechanisms related to the potential mismatch between the 5*d* element and Al. These studies show the importance of extrinsic mechanisms derived from potential mismatch as a route to obtaining large spin Hall angles with high technological impact. Indeed, it is demonstrated that a state-of-the-art racetrack device has a several-fold increased current-induced domain wall efficiency using these materials as compared to prior-art materials.

1. Introduction

Spintronics is driven by the generation of spin currents and especially their use as spin torques in manipulating magnetization.[1–5] This is the principal mechanism for writing magnetic memory bits in magnetic random-access memories (MRAMs)[6] and in moving magnetic bits, namely domain walls (DWs) in magnetic racetrack memories.[7,8] Spin currents can be generated from charge currents via the spin Hall effect (SHE). There has been much interest in certain classes of high-quality, crystalline compounds that could give rise to large SHEs that originate from the intrinsic electronic band structures of such materials:[9,10] such materials include topological insulators,[11–13] and Dirac and Weyl semimetals.[14–16] However, here, we show very large SHEs arising rather from extrinsic scattering in highly resistive alloys formed from a 5*d* element and aluminum at room temperature that are highly useful for practical applications.

The spin–orbit interaction (SOI) plays a central role in the SHE such that, typically, the larger the atomic number Z, the larger is the SHE. Furthermore, the bigger the contrast between Z of the constituent elements in a compound or alloy, the larger will be the extrinsic scattering and, consequently, the SHE.[17,18] In this regard, alloying light metals such as aluminum with a 5*d* transition metal is anticipated to generate a large extrinsic SHE.[19] Here, we show that M_xAl_{100-x} (M = Ta, W, Re, Os, Ir, and Pt) alloys exhibit dramatic changes in not only the resistivity ρ but also the spin Hall angle (SHA) θ_{SH} and spin Hall (SHC) σ_{SH} as a function of their composition, x. We find that there is, in many cases, a transition from a highly disordered, near amorphous phase, to a highly crystalline phase at a critical composition. Furthermore, we find that the resistivity and SHA exhibit the largest values near the amorphous-crystalline boundary in which extrinsic scattering is maximized. To support this conjecture, we find that the magnitude of the maximum resistivity and the corresponding SHA vary systematically with Z. This shows that the filling of the 5*d* shell plays a critical role, such that the resistivity and SHA are related to the number of unpaired electrons in the 5*d* shell of M, so that ρ exhibits a maximum value for M = Re or Os (number of unpaired d electrons due to Hund's rule = 5, 6, respectively). We find that the resistivity is approximately linearly proportional to the SHA, so that the power consumption ($\approx \rho/\theta_{SH}^2$) that varies inversely with θ_{SH} is minimized for maximum SHA.[20] Hence, we find that M_xAl_{100-x} are excellent sources of spin–orbit torque (SOT) sources with smaller power

P. Wang, A. Migliorini, S.-H. Yang, J.-C. Jeon, I. Kostanovskiy, H. Meyerheim, H. Han, H. Deniz, S. S. P. Parkin
Max Planck Institute for Microstructure Physics
06120 Halle, Germany
E-mail: stuart.parkin@mpi-halle.mpg.de
P. Wang, S. S. P. Parkin
Institute of Physics
Martin Luther University Halle-Wittenberg
06120 Halle, Germany

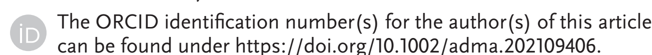
The ORCID identification number(s) for the author(s) of this article can be found under https://doi.org/10.1002/adma.202109406.

© 2022 The Authors. Advanced Materials published by Wiley-VCH GmbH. This is an open access article under the terms of the Creative Commons Attribution License, which permits use, distribution and reproduction in any medium, provided the original work is properly cited.

DOI: 10.1002/adma.202109406

consumptions, compared to established spin Hall metallic elements. On the other hand, we find that when the 5*d* shell is fully filled, i.e., M = Au, no significant changes in ρ and θ_{SH} as a function of x are found, thereby confirming that the unpaired orbitals in the 5*d* shell plays a key role in the formation of scattering potentials for ρ and the extrinsic SHE.

2. Results and Discussion

2.1. Crystal Structure and Resistivity of M_xAl_{100-x} Alloys

The M_xAl_{100-x} films used in this study were prepared using dc magnetron co-sputtering from a 5*d* metal M target and an Al sputter target to deposit M_xAl_{100-x} films on top of a [001]-oriented MgO substrate in an ultrahigh vacuum chamber. The composition was varied for x varying from ≈10 to ≈90 atom.% by varying the power applied to each of the targets. Typical deposition rates were 0.5–2 Å s^{-1} and the films were deposited at room temperature. On top of these films were grown magnetic layers to form magnetic racetracks or to form structures suitable for spin-torque ferromagnetic resonance (ST-FMR) studies. The structures were protected from oxidation by a 4 nm thick MgO layer capping layer (see Experimental Section for details). The sheet resistances R_S of the as-grown films are measured by a four-point in-line probe method, from which ρ is obtained from the relationship $\rho = R_s t$, where t is the film thickness. The crystal structures of the films were investigated by X-ray diffraction (XRD) and cross-section transmission electron microscopy (XTEM).

The XRD experiments were carried out with a four-circle diffractometer using Cu-K-α1 radiation and employing a 2D pixel detector. The data shown in Figure S1 (Supporting Information) were collected in the symmetric θ–2θ scan mode corresponding to longitudinal scans along the [001] direction in reciprocal space. The structure of all the alloys, with the exception of Ta–Al, was found to vary systematically with x, from a poorly crystalline, nearly amorphous structure for small x to a highly textured, crystalline structure for x larger than a critical value, x_{crit} ≈ 20–40 at%, that depends on M. As M is varied systematically along the 5*d* period we find a systematic trend to form a well-ordered crystalline phase with an increasing number of 5*d* electrons. For the early elements, Ta and Re, only poorly ordered phases are observed almost independent of x (see Figure S1a,c, Supporting Information), while for W we find only the (002) reflection of the bulk-like, completely chemically, disordered phase with space group (SGR) symmetry Im$\overline{3}$m in the region between x = 53 and 93 at%. By contrast, the late d-transition elements (Os, Ir, Pt, and Au) form increasingly well-ordered structures of the CsCl type (SGR symmetry Pm$\overline{3}$m, often labeled $L1_0$), as shown in **Figure 1**a. For instance, a detailed analysis of the Ir_xAl_{100-x} alloys with intermediate values of x indicates the almost perfect ordering of the elements on the distinct lattice sites (000) and (½ ½ ½), where only ≈10–15 at% of Ir (Al) are exchanged with the Al (Ir) sites (for more details see Supporting Information).

In all cases where a crystalline CsCl-type structure is formed at intermediate values of x, a resistivity maximum is observed at the onset of the long-range order, which is identified at x lying in the range of about x = 20–40 at%, depending on M (Figure 1b,c). This concentration likely corresponds to a "percolation limit" where the metal number density exceeds a critical value where the average M–M distance and interaction becomes large enough to establish a long-range ordered structure.[21,22] This coincides with the resistivity maximum as the crystalline domains are still small and the number of grain boundaries is large. The maximum value of ρ ≈ 1100 μΩ cm is observed for $Os_{22}Al_{78}$. The peak values of the resistivity are considerably higher than the end members in each M–Al case (≈3 μΩ cm for Al and Au and 5–20 μΩ cm for the other M).

Beyond this critical concentration, the resistivity decreases as the size of the coherently scattering domains and the degree of chemical ordering increases. The latter is directly evidenced by the narrowing of the X-ray reflections (e.g., Figure S1e for x = 50 at% and Figure S1g for x = 41 at%, Supporting Information). Structural ordering can be estimated by the ratio between the intensities of the (001) and the (002) reflections that has a maximum (i.e., maximum ordering within the CsCl-type structure) for x (at%) in the range ($33 < x < 58$) for Ir_xAl_{100-x} as well as for Pt_xAl_{100-x} in the range $32 < x < 50$. Finally, in the high-x limit, we observe for the Ir_xAl_{100-x} another phase transition to a Fm$\overline{3}$m symmetry Ir metal phase (see Figure S1f, Supporting Information), in which the Al atoms can be viewed as diluted within the Ir matrix.

The c lattice parameter systematically increases with increasing x within the crystalline phase region, as shown in Figure 1d. For example, for Ir_xAl_{100-x}, c increases by ≈10% as x is increased from 33 to 61 at%, consistent with an enhanced tetragonality. For x = 50 at% cross-sectional transmission electron microscopy shows a highly ordered crystalline phase consistent with the $L1_0$ structure, as shown for $Ir_{50}Al_{50}$ in Figure 1e.

2.2. Evaluation of SHA

The charge-to-spin conversion efficiency, i.e., the SHA θ_{SH} of the M_xAl_{100-x} materials are measured in patterned device structures formed from M_xAl_{100-x} (43 Å) | $Co_{20}Fe_{60}B_{20}$ (CFB) (60 Å) using a ferromagnetic layer of CFB and a ST-FMR technique (**Figure 2**a) at ambient temperature by analyzing FMR linewidths as a function of DC bias current[23] (see Supporting Information for details). Note that the measured θ_{SH} corresponds to an effective θ_{SH} that includes the interface transparency[24] between M–Al and the CFB ferromagnetic layer that will result in a reduction in the spin current that can cross this interface (and, therefore, the extracted SHA) (see Figure S3–S9, Supporting Information). A very important finding is that, as shown in Figure 2b, θ_{SH} increases systematically with the resistivity in the poorly crystalline phase of the M_xAl_{100-x} films. The maximum value of θ_{SH} ≈ 1.04 is found in Os–Al at the composition that displays the largest value of ρ. As for the highly textured $L1_0$ phase in both Os_xAl_{100-x} and Ir_xAl_{100-x}, θ_{SH} also increases with their resistivity, just as in the amorphous phase, while θ_{SH} for Pt_xAl_{100-x} decreases slightly as ρ increases, as shown in Figure 2c. The values of θ_{SH} are very large and considerably larger than those that have been reported for the pure elements Pt,[23] Ta,[25] or W,[26] and also oxidized W that displays perhaps the largest value of θ_{SH} yet reported (≈–0.5).[27]

 © 2022 The Authors. Advanced Materials published by Wiley-VCH GmbH

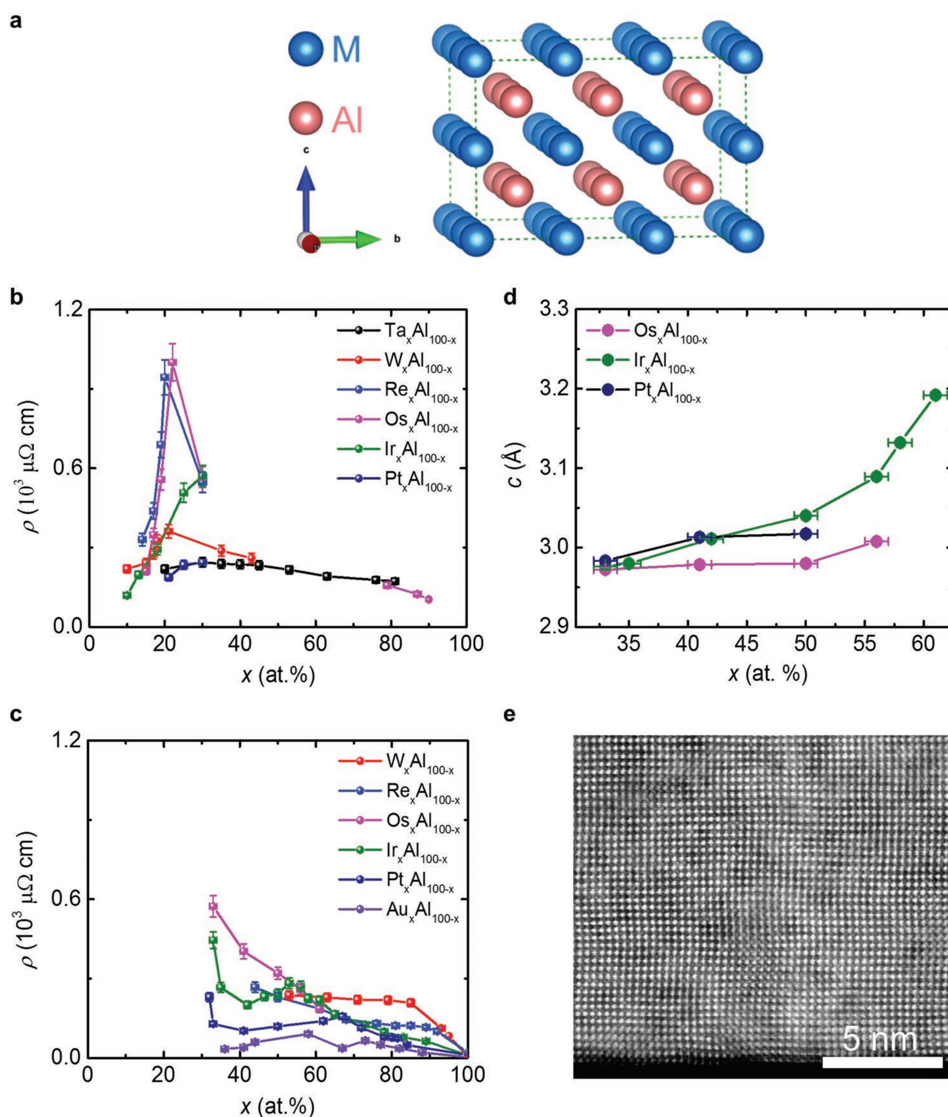

Figure 1. Crystal structure and electronic properties. a) Schematic diagram of the chemically ordered CsCl-type *M*–Al structure (*M* = Os, Ir, and Pt). b,c) Sheet resistivity of M_xAl_{100-x} with a poorly crystalline phase (b), and a highly textured crystalline phase (c) as a function of *x*, respectively. d) Out-of-plane lattice parameter *c* as a function of *x* for Os_xAl_{100-x}, Ir_xAl_{100-x} and Pt_xAl_{100-x} with the $L1_0$ structure. e) High-angle annular dark-field scanning transmission electron microscopy (HAADF-STEM) image of a 300 Å-thick $Ir_{50}Al_{50}$ thin film.

The values of the effective θ_{SH} found for the member of each M_xAl_{100-x} series of compounds with the maximum resistivity are plotted in Figure 2d versus the atomic number *Z*. For both *M* = Os and Ir, values of θ_{SH} significantly close or larger than 1 are found. Interestingly, ρ displays a similar dependence on *Z* as does θ_{SH}. These data clearly show that the filling of the 5*d*-shell plays a key role in the electrical conductivity and charge-to-spin conversion. Note that the power consumption in spin-torque processes has been shown to vary as ρ/θ_{SH}^2.[20] This quantity is plotted versus *Z* in Figure 2e, showing that the power consumption is minimized near the atomic number at which ρ and θ_{SH} are maximized. Finally, the SHC $\sigma_{SH} = \theta_{SH} \times \sigma$, which is plotted in Figure 2f vs *Z*, increases monotonically with Z reaching a maximum and very high value of 2.34 ± 0.61 (10^5 $\hbar$/2e Ω^{-1} m^{-1}) in $Pt_{41}Al_{59}$ (Figure 2f), which is comparable with the previously reported value 2.0 (10^5 $\hbar$/2e Ω^{-1} m^{-1}) from $Pt_{80}Al_{20}$.[28]

2.3. Current Induced DW Motion in IrAl–Synthetic Antiferromagnets (SAFs)

As mentioned earlier, the SHE finds a very important application in the manipulation of magnetization via spin torques derived from spin currents.[29,30] We have applied our finding of giant SHEs in M_xAl_{100-x} films to the current induced motion of DWs in SAF racetrack layers, which have been shown to display the highest current-induced DW velocities.[31] We consider the case of several Ir–Al alloys as the source of the spin current and we form SAF racetracks from Co/Ni/Co trilayer structures grown on top of the $L1_0$-ordered IrAl alloy layer. Interestingly, we find that the Co and Ni layers grow oriented [001] with excellent lattice matching (see Figure S14, Supporting Information). This is distinct from typical cases in which Co and Ni layers are oriented along [111] when grown on Pt or Ir layers. Furthermore,

 © 2022 The Authors. Advanced Materials published by Wiley-VCH GmbH

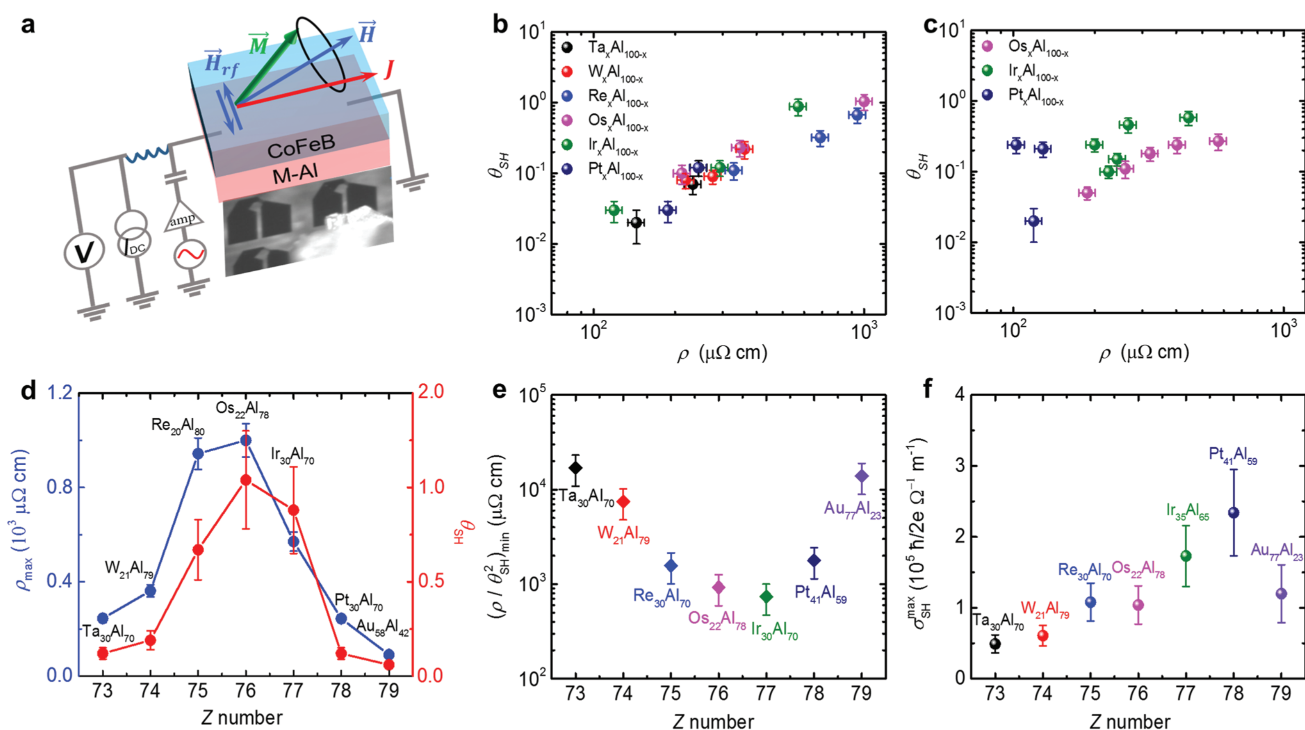

Figure 2. ST-FMR measurements of $M_xAl_{100-x}|Co_{20}Fe_{60}B_{20}$ devices. a) Illustration of the ST-FMR experimental setup. b) Effective θ_{SH} as a function of resistivity for several M_xAl_{100-x} compounds which display poor crystallinity. c) Effective θ_{SH} as a function of resistivity for M_xAl_{100-x} with an $L1_0$ crystalline structure. d) Maximum resistivity and effective θ_{SH} at the same x for M_xAl_{100-x} as a function of atomic number Z. e) The minimum ratio of ρ/θ_{SH}^2 of M_xAl_{100-x} as a function of Z. f) Maximum SHC σ_{SH} in $M_xAl_{100-x}|Co_{20}Fe_{60}B_{20}$ samples as a function of Z.

we find that the Ir–Al|Co|Ni|Co stacks display excellent perpendicular magnetic anisotropy and a large anomalous Hall resistance ($R_H \approx 4\ \Omega$) (Figure S14, Supporting Information). Finally, note that we use RuAl as an antiferromagnetic coupling spacer layer instead of Ru since RuAl also forms an $L1_0$-structure on [001]-oriented MgO substrates (Figure S15, Supporting Information). The complete film stack of Ir_xAl_{100-x}|3 Co|7 Ni|2.5 Co|8 RuAl|3 Co|7 Ni|3 Co (thickness in Å) shows an [001] orientation throughout the whole stack (Figure S16a, Supporting Information). The hysteresis loops of these stacks exhibit out-of-plane magnetized spin-flop transitions, thereby showing that the RuAl spacer layer induces a strong antiferromagnetic exchange coupling between the two Co/Ni/Co ferromagnetic layers (**Figure 3**b). The ratio of the remanent (M_R) to saturation magnetization (M_S) is measured to be ≈0.08, close to zero for an ideal SAF structure. The $\frac{M_R}{M_S}$ ratio reveals a strong dependence on the Ir_xAl_{100-x} composition (see Figure S16, Supporting Information) that we suppose is related to proximity induced moment in the Ir–Al layer.

To investigate the current-induced DW motion, micrometer-wide wires with different lengths and widths are fabricated by photolithography and Ar ion milling (an optical image of a typical device is shown in Figure 3c). Kerr microscopy is used to monitor the position of individual DWs after the application of a succession of 5 ns-long current pulses (see Experimental Section for details). The dependence of the DW velocity, v, on the current density, J, is plotted in Figure 3d for Ir_xAl_{100-x} where x is varied from 35 to 58 at%. Very large DW velocities are found due to a large exchange coupling torque:[32] the largest DW velocity is measured to be ≈650 m s^{-1} at $J \approx 6 \times 10^7$ A cm^{-2} for $Ir_{42}Al_{58}$. We note that this corresponds to an efficiency that is 3 to 5 times greater than that reported in conventional [111]-textured SAFs based on Co, Ni, and Ru layers grown on Pt underlayers. Moreover, the threshold current density, J_{th}, above which the DW starts to move is measured to be ≈5×10^6 A cm^{-2} for $Ir_{35}Al_{65}$ that is considerably lower than previously reported in Ru-based SAF structures prepared on Pt layers.[31] The dependence of J_{th} and σ_{SH} on Ir content in Ir_xAl_{100-x} shows that J_{th} decreases with increasing σ_{SH} consistent with an increasing SOT (Figure 3e).

The SOT is known to be very sensitive to the detailed structure of the interface between the SOT layer and the magnetic layer.[33] For example, as shown in Figure 3f, 2 Å thick Ir or Al layers inserted at this interface significantly changes the dependence of v on the current density. The insertion of the Al dusting layer results in a lower terminal value of $v \approx 200$ m s^{-1} while J_c does not change. On the other hand, the insertion of the Ir dusting layer shifts the v–J curve to higher J thus increasing J_c. These observations can be accounted for by: i) a decrease in the Dzyaloshinskii–Moriya interaction (DMI) by the insertion of an Al dusting layer as compared with the insertion of an Ir dusting layer;[34] ii) a decrease in the exchange coupling torque[31] due to the increased ratio of M_R/M_S for the Al insertion layers as compared with the Ir insertion layers, as shown in Figure S18 (Supporting Information); iii) an increase in spin memory loss ($\delta = t/l_{sf}$, t is the thickness of the dusting layer, and l_{sf} is the spin diffusion length) arising from the strong

© 2022 The Authors. Advanced Materials published by Wiley-VCH GmbH

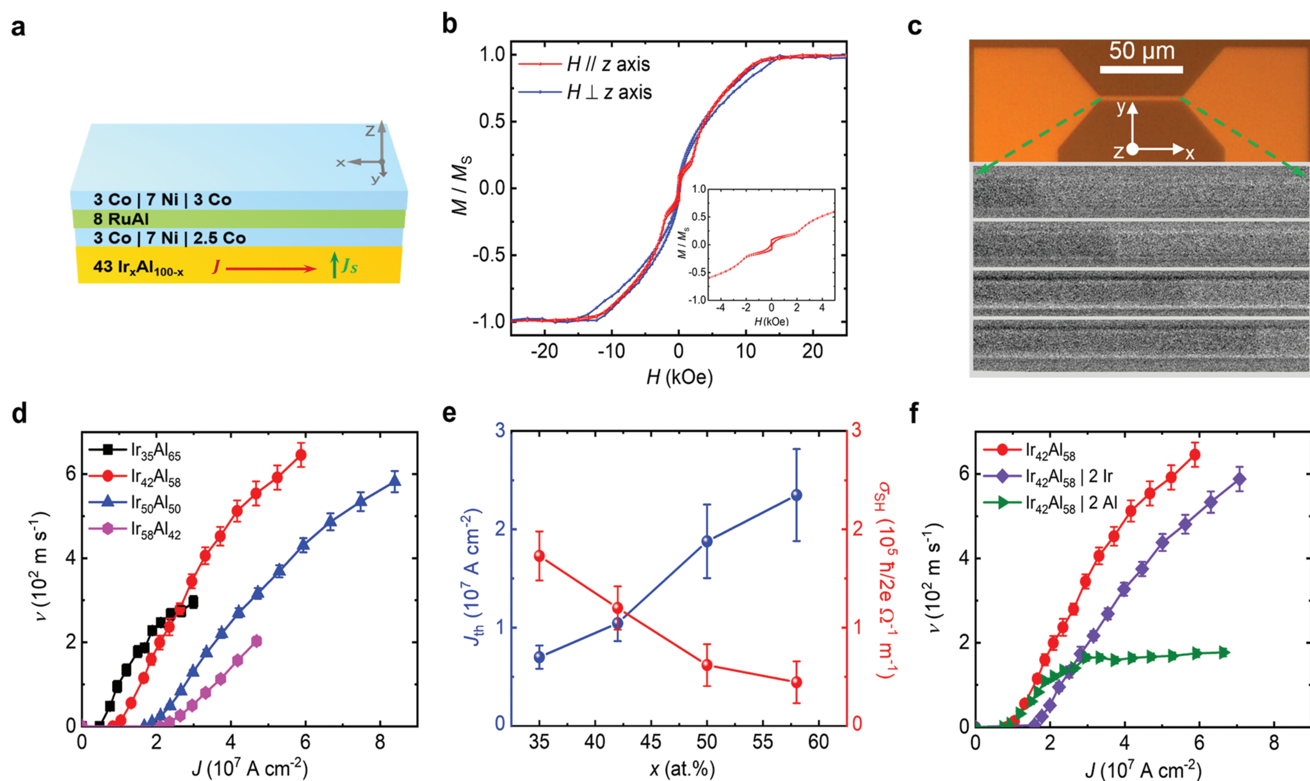

Figure 3. Current-induced DW motion in Ir_xAl_{100-x} SAF racetracks. a) Schematic of SAF multilayer with an Ir_xAl_{100-x} underlayer. b) Out-of-plane (red) and in-plane (blue) magnetic hysteresis loops for 43 Å $Ir_{50}Al_{50}$ | SAFs with the out-of-plane *M*–*H* loop shown in the inset. c) Optical microscopy image of the racetrack device and Kerr microscopy differential images showing the propagation of a single domain wall along the track, in response to a sequence of 5 ns-long current pulses ($J \approx 1.2 \times 10^8$ A cm^{-2}). d) DW velocity v versus pulse current density J in nanowires formed from 43 Å Ir_xAl_{100-x} | SAFs. e) Critical threshold current density (J_{th}) to drive the DWs in Ir_xAl_{100-x} | SAF structures, and SHC of Ir_xAl_{100-x} as a function of x. f) DW velocity versus pulse current density in nanowires formed from 43 Å $Ir_{42}Al_{58}$ | no dusting layer and dusting layer of 2 M (M = Ir and Al) | SAFs.

spin–orbit interaction of Ir that degrades the strength of the SOT as compared with the weaker SOI from Al that displays a very long spin diffusion length.[35,36,37] The degradation of the SOT leads to an increase of J_c for the Ir insertion layers.

2.4. SOT Switching of IrAl-SAFs

To further evaluate the SHE from Ir–Al, we carry out SOT-switching experiments using standard Hall bars[25] formed from an SAF structure (see the inset of **Figure 4**a and Supporting Information for the details). The Hall resistance, which is swept along the magnetic easy-axis (out-of-plane), is plotted in Figure 4b, showing a well-defined spin-flop transition. Current pulses are applied along the Hall bar as an external magnetic field applied along the current direction is switched between ≈±500 Oe (Figure 4c). The change in Hall resistance equals that for the magnetic field induced switching (Figure 4b) for the field range from ≈+3 kOe to ≈–3 kOe), thereby showing a complete switching of the SAF layer at $J \approx \pm 7$ MA cm^{-2}, which is a smaller critical current density than needed for realistic applications.[3] The flipping of the Hall resistance upon reversal of the in-plane field direction confirms the SOT switching of the magnetic layers.[38] To investigate the reproducibility and reliability of the current induced switching, the switching experiments were repeated ≥10 000 times without any failure, as shown in Figure 4d–f (see Experimental Section and Supporting Information for further details).

3. Conclusions

Alloys of 5*d* elements with light elements are shown to give rise to very large SHAs that exceed those of the best known non-topological materials to date. The largest values of ρ and θ_{SH} are observed to be ≈1100 μΩ cm and 1.04, respectively, in the alloy $Os_{22}Al_{78}$, while the largest value of σ_{SH} is found to be 2.34 (10^5 $\hbar/2e$ Ω^{-1} m^{-1}) in $Pt_{41}Al_{59}$. Moreover, these materials can be prepared by straightforward sputter deposition techniques, rather than molecular beam epitaxy methods, and, furthermore, act as a template for the growth of highly crystalline textured magnetic layers and heterostructures that are the basis of several emerging magnetic nonvolatile memory and storage technologies. We demonstrate that using Ir–Al as the source of spin current, highly efficient chiral DW motion is found in SAF racetracks with a very low threshold current density. An important finding is that the largest SHAs are found at compositions that lie close to a phase boundary where the structure loses its crystalline texture, and, that the magnitude of the SHA scales with the resistivity of the 5*d*-alloy, clearly demonstrating the

© 2022 The Authors. Advanced Materials published by Wiley-VCH GmbH

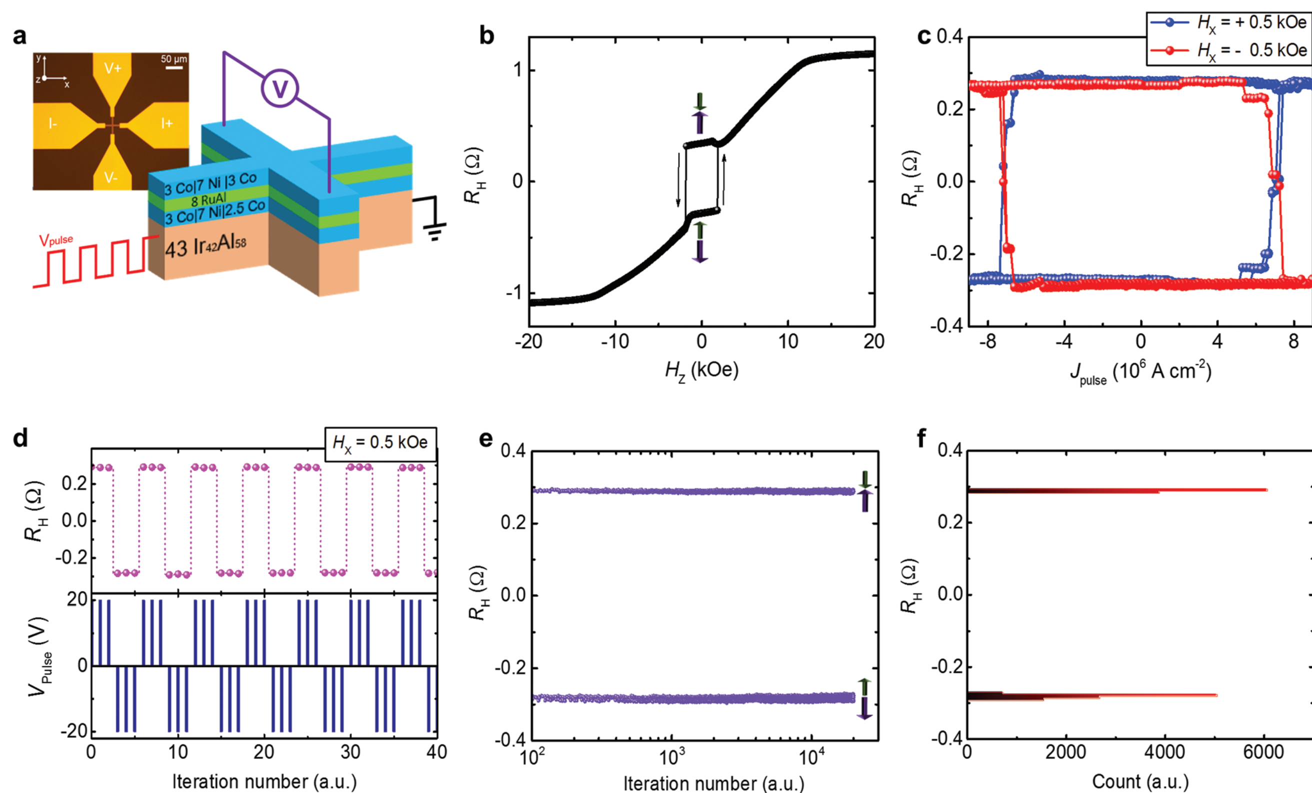

Figure 4. SOT magnetization switching. a) Schematic diagrams of sample stack and Hall bar devices. b) Anomalous Hall resistance (R_H) as a function of out-of-plane magnetic field H in 43 Å $Ir_{42}Al_{58}$ | SAF structures measured at 300 K. c) Magnetization switching of 43 Å $Ir_{42}Al_{58}$ | SAF with in-plane field of ±500 Oe at 300 K. d) Deterministic magnetization switching in 43 Å $Ir_{42}Al_{58}$ | SAF devices by a series of ≈±20 V pulses. e) R_H switched by a series of positive and negative voltage pulses as a function of iteration number. f) Deterministic switching of R_H.

extrinsic origin of the SHE. Finally, the power consumption for SOT switching is minimized for the most resistive alloys. Our findings show that the giant SHEs and SOTs in M_xAl_{100-x} alloys can provide an excellent platform for potential applications in diverse memory and logic devices with highly efficient interconversion of charge-to-spin currents and low power consumption.

4. Experimental Section

Sample Preparation, Characterization, and Device Fabrication: The films were deposited in an AJA "Flagship Series" sputtering system onto 10 × 10 mm^2 MgO (100) substrates. The base pressure before the deposition was ≤10^{-8} Torr and the Ar gas pressure during deposition was 3 mTorr. The M_xAl_{100-x} and RuAl films were prepared by co-sputtering from heavy metal and Al targets. The $Co_{20}Fe_{60}B_{20}$ layer was prepared by sputtering from a single target with a composition of $Co_{20}Fe_{60}B_{20}$. Highly resistive 50 Å thick TaN-capping layers were fabricated by introducing 20% N_2 into the Ar sputtering gas. The composition of the M_xAl_{100-x} layers was determined by Rutherford backscattering spectrometry (RBS) with an accuracy of ≈1–2 at%. High-resolution XRD measurements were performed using a Bruker D8 Discover system with Cu Kα_1 radiation (λ = 1.54 Å) at room temperature. Magnetization hysteresis loops were measured using a superconducting quantum interference device vibrating sample magnetometer (SQUID-VSM). Lamella were prepared for XTEM with focused ion beam milling using a Tescan GAIA3 instrument. TEM data were measured in an FEI Titan 80–300 (scanning) TEM equipped with a CEOS CESCOR third-order axial geometric aberration corrector and a Gatan UltraScan 1000 slow-scan CCD camera. The primary electron energy was 300 kV. Device fabrication was carried out using optical lithography and ion beam etching. Subsequently, 3nm thick Ti and 80 nm thick Au electrical contact layers were deposited using a lift-off process. The resistance of the M_xAl_{100-x} films was measured using a Veeco FPP5000 four-point probe station. The thickness of the M_xAl_{100-x} thin films was measured using a Bruker Dimensional Icon atomic force microscope.

Spin-Torque Ferromagnetic Resonance: ST-FMR measurements were performed at room temperature in micro-strip devices of various sizes. A gigahertz frequency probe tip (Picoprobe Model 40A) was used to inject an RF excitation current (Keysight MXG N5183B signal generator) at a power of 20 dBm. The rectified DC voltage across the micro-strip was simultaneously measured using a bias-tee (Tektronix PSPL5545) and a nanovoltmeter (Keithley 2182A). The rectified DC voltage resulting from the mixing of the RF current with the varying resistance of the micro-strip due to the anisotropic magnetoresistance of the $Co_{20}Fe_{60}B_{20}$ layer gives rise to the FMR signal. The FMR signal at a particular excitation frequency was measured as the external in-plane magnetic field was swept, at an angle of 45° to the long axis of the micro-strip. The DC bias current was applied from −2 to 2 mA with an RF-current with a frequency of 9 GHz to extract the half-width of the ferromagnetic resonance peak to obtain the effective spin Hall angle.

Measurement of DW Velocity: Kerr optical microscopy in differential mode was used to monitor the position of the DW along the nanowire in response to a series of current pulses. The sensitivity of this technique was sufficient to detect the motion of single DWs in nanowires as narrow as ≈100 nm. Images were taken after a fixed number of current pulses chosen such that the DW had moved by a significant distance, typically ≈1–2 µm. The DW velocity was then determined by assuming that the DW moves only during pulses. A linear fit of the DW position versus the integrated current pulse length t_{CP} was used, that is, the product of pulse duration and the number of pulses applied. In some

© 2022 The Authors. Advanced Materials published by Wiley-VCH GmbH

cases, the DW may be pinned by a local defect until enough pulses were applied to dislodge it. In these cases, only the portions of the curve were fitted in which the DW position depends linearly on t_{CP}. The standard deviation of the differential velocity, that is, the point-by-point derivative of the DW position versus t_{CP} curve, was used to determine an error bar. Note that the DW velocity was defined to be positive (negative) when the DWs move along the current (against) flow.

Electronic Transport Measurements: Electrical transport measurements, including (ST-FMR), Hall measurement, and electrical switching measurement, were performed at room temperature. For conventional Hall measurements, a DC current source (Keithley 6221) and a nanovoltmeter (Keithley 2182a) were used. Electrical switching experiments using ms-long current pulses were made with a multifunctional source meter (Keithley 2635B). More details are given in Supporting Information.

Statistical Analysis: 1) Pre-processing of data: $\sigma = 1/\rho$, M/M_s (M_s is saturation magnetization, M is magnetization versus magnetic field). 2) $SD = \sqrt{\frac{\sum(x-\bar{x})^2}{n-1}}$, $\bar{x} = \frac{(\sum x)}{n}$, 3) Sample size ($n$) is 5. 4) Two-sided testing with alpha value (0.05) and p-value (0.5734). 5) Software used for statistical analysis: Origin 2019.

Supporting Information

Supporting Information is available from the Wiley Online Library or from the author.

Acknowledgements

The authors acknowledge support from the EU ASPIN program and from the Samsung Electronics R&D program “Material and Device research on Racetrack Memory” at the MPI of Microstructure Physics.

Open access funding enabled and organized by Projekt DEAL.

Conflict of Interest

The authors declare no conflict of interest.

Author Contributions

S.S.P.P. conceived and supervised the project. P.W. grew the films, characterization, and patterned devices. A.M. conducted domain wall motion measurements. P.W performed transport measurements and analyzed the data with input from S.H.Y., A.M., J.J., H.H., H.M., and S.S.P.P. H.M. conducted detailed XRD analysis of the 5*d*-Al alloy thin films. I.K. conducted RBS measurements of the M_xAl_{100-x} samples. H.D. performed TEM measurements. P.W, S.H.Y, and S.S.P.P wrote the manuscript. All authors participated in discussing the data and writing the manuscript.

Data Availability Statement

The data that support the findings of this study are available from the corresponding author upon reasonable request.

Keywords

5*d* transition metal–Al alloys, spin Hall effect, spin–orbit torque, racetrack memories

Received: November 19, 2021
Revised: March 22, 2022
Published online:

[1] J. Sinova, S. O. Valenzuela, J. Wunderlich, C. H. Back, T. Jungwirth, *Rev. Mod. Phys.* **2015**, *87*, 1213.
[2] A. Manchon, J. Železný, I. M. Miron, T. Jungwirth, J. Sinova, A. Thiaville, K. Garello, P. Gambardella, *Rev. Mod. Phys.* **2019**, *91*, 035004
[3] Q. Shao, P. Li, L. Liu, H. Yang, S. Fukami, A. Razavi, H. Wu, F. Freimuth, Y. Mokrousov, M. D. Stiles, S. Emori, A. Hoffmann, J. Åkerman, K. Roy, J.-P. Wang, S.-H. Yang, K. Garellob, W. Zhang, *IEEE Trans. Magn.* **2021**, *57*, 800439.
[4] S.-H. Yang, *Appl. Phys. Lett.* **2020**, *116*, 120502
[5] S.-H. Yang, R. Naaman, Y. Paltiel, S. S. P. Parkin, *Nat. Rev. Phys.* **2021**, *3*, 328.
[6] S. Ikegawa, F. B. Mancoff, J. Janesky, S. Aggarwal, *IEEE Trans. Electron Devices* **2020**, *67*, 1407.
[7] S. Parkin, S.-H. Yang, *Nat. Nanotechnol.* **2015**, *10*, 195.
[8] S. S. P. Parkin, M. Hayashi, L. Thomas, *Science* **2008**, *320*, 190.
[9] Z. Chi, Y.-C. Lau, X. Xu, T. Ohkubo, K. Hono, M. Hayashi, *Sci. Adv.* **2020**, *6*, eaay2324.
[10] M. Dc, R. Grassi, J.-Y. Chen, M. Jamali, D. R. Hickey, D. Zhang, Z. Zhao, H. Li, P. Quarterman, Y. Lv, M. Li, A. Manchon, K. A. Mkhoyan, T. Low, J.-P. Wang, *Nat. Mater.* **2018**, *17*, 800.
[11] M. Mogi, K. Yasuda, R. Fujimura, R. Yoshimi, N. Ogawa, A. Tsukazaki, M. Kawamura, K. S. Takahashi, M. Kawasaki, Y. Tokura, *Nat. Commun.* **2021**, *12*, 1404.
[12] K. Kondou, R. Yoshimi, A. Tsukazaki, Y. Fukuma, J. Matsuno, K. S. Takahashi, M. Kawasaki, Y. Tokura, Y. Otani, *Nat. Phys.* **2016**, *12*, 1027.
[13] H. Wu, P. Zhang, P. Deng, Q. Lan, Q. Pan, S. A. Razavi, X. Che, L. Huang, B. Dai, K. Wong, X. Han, K. L. Wang, *Phys. Rev. Lett.* **2019**, *123*, 207205.
[14] B. Zhao, D. Khokhriakov, Y. Zhang, H. Fu, B. Karpiak, A. Md Hoque, X. Xu, Y. Jiang, B. Yan, S. P. Dash, *Phys. Rev. Res.* **2020**, *2*, 013286.
[15] N. P. Armitage, E. J. Mele, A. Vishwanath, *Rev. Mod. Phys.* **2018**, *90*, 015001.
[16] N. Nagaosa, T. Morimoto, Y. Tokura, *Nat. Rev. Mater.* **2020**, *5*, 621.
[17] Y. Niimi, Y. Kawanishi, D. H. Wei, C. Deranlot, H. X. Yang, M. Chshiev, T. Valet, A. Fert, Y. Otani, *Phys. Rev. Lett.* **2012**, *109*, 156602.
[18] X. Shu, J. Zhou, J. Deng, W. Lin, J. Yu, L. Liu, C. Zhou, P. Yang, J. Chen, *Phys. Rev. Mater.* **2019**, *3*, 114410.
[19] Y.-C. Lau, T. Seki, K. Takanashi, *APL Mater.* **2021**, *9*, 081113.
[20] J. Han, A. Richardella, S. A. Siddiqui, J. Finley, N. Samarth, L. Liu, *Phys. Rev. Lett.* **2017**, *119*, 077702.
[21] P. Jensen, A.-L. Barabási, H. Larralde, S. Havlin, H. E. Stanley, *Chaos, Solitons Fractals* **1995**, *6*, 227.
[22] P. Šmilauer, *Contemp. Phys.* **1991**, *32*, 89.
[23] L. Liu, T. Moriyama, D. C. Ralph, R. A. Buhrman, *Phys. Rev. Lett.* **2011**, *106*, 036601.
[24] W. Zhang, W. Han, X. Jiang, S.-H. Yang, S. S. P. Parkin, *Nat. Phys.* **2015**, *11*, 496.
[25] L. Liu, C.-F. Pai, Y. Li, H. W. Tseng, D. C. Ralph, R. A. Buhrman, *Science* **2012**, *336*, 555.
[26] J. Liu, T. Ohkubo, S. Mitani, K. Hono, M. Hayashi, *Appl. Phys. Lett.* **2015**, *107*, 232408.
[27] K.-U. Demasius, T. Phung, W. Zhang, B. P. Hughes, S.-H. Yang, A. Kellock, W. Han, A. Pushp, S. S. P. Parkin, *Nat. Commun.* **2016**, *7*, 10644.
[28] M.-H. Nguyen, M. Zhao, D. C. Ralph, R. A. Buhrman, *Appl. Phys. Lett.* **2016**, *108*, 242407.

© 2022 The Authors. Advanced Materials published by Wiley-VCH GmbH

[29] K.-S. Ryu, L. Thomas, S.-H. Yang, S. Parkin, *Nat. Nanotechnol.* **2013**, *8*, 527.
[30] K.-S. Ryu, S.-H. Yang, L. Thomas, S. S. P. Parkin, *Nat. Commun.* **2014**, *5*, 3910.
[31] S.-H. Yang, K.-S. Ryu, S. Parkin, *Nat. Nanotechnol.* **2015**, *10*, 221.
[32] R. Bläsing, T. Ma, S.-H. Yang, C. Garg, F. K. Dejene, A. T. N'Diaye, G. Chen, K. Liu, S. S. P. Parkin, *Nat. Commun.* **2018**, *9*, 4984.
[33] Y. Guan, X. Zhou, T. Ma, R. Bläsing, H. Deniz, S.-H. Yang, S. S. P. Parkin, *Adv. Mater.* **2021**, *33*, 2007991.
[34] F. Ajejas, V. Křižáková, D. S. Chaves, J. Vogel, P. Perna, R. Guerrero, A. Gudin, J. Camarero, S. Pizzini, *Appl. Phys. Lett.* **2017**, *111*, 202402.
[35] K. Gupta, R. J. H. Wesselink, R. Liu, Z. Yuan, P. J. Kelly, *Phys. Rev. Lett.* **2020**, *124*, 087702.
[36] T. Fache, J. C. Rojas-Sanchez, L. Badie, S. Mangin, S. Petit-Watelot, *Phys. Rev. B* **2020**, *102*, 064425.
[37] J. Bass, W. P. Pratt, *J. Condens. Matter Phys.* **2007**, *19*, 183201.
[38] P. X. Zhang, L. Y. Liao, G. Y. Shi, R. Q. Zhang, H. Q. Wu, Y. Y. Wang, F. Pan, C. Song, *Phys. Rev. B.* **2018**, *97*, 214403.

© 2022 The Authors. Advanced Materials published by Wiley-VCH GmbH